INL/JOU-23-72858-Revision-0

Boosting the performances of protonic solid oxide fuel cells for co-production of propylene and electricity from propane by integrating thermo- and electro-catalysis

Changing the World's Energy Future

Ruifang Zhang, Wenzhuo Wu, Wei Wu, Lucun Wang, Yuqing Meng, Dong Ding, Min Wang

Idaho National Laboratory

INL/JOU-23-72858-Revision-0

Boosting the performances of protonic solid oxide fuel cells for co-production of propylene and electricity from propane by integrating thermo- and electro- catalysis

Ruifang Zhang, Wenzhuo Wu, Wei Wu, Lucun Wang, Yuqing Meng, Dong Ding, Min Wang

February 2024

Idaho National Laboratory
Idaho Falls, Idaho 83415

http://www.inl.gov

Prepared for the
U.S. Department of Energy
Under DOE Idaho Operations Office
Contract DE-AC07-05ID14517

Fuel xxx (xxxx) 129685

Contents lists available at ScienceDirect

Fuel

journal homepage: www.elsevier.com/locate/fuel

Full Length Article

Boosting the performances of protonic solid oxide fuel cells for co-production of propylene and electricity from propane by integrating thermo- and electro- catalysis

Ruifang Zhang [a, b, 1], Yuqing Meng [a, 1], Lu-Cun Wang [a, *], Min Wang [a, c], Wei Wu [a], Wenzhuo Wu [b, *], Dong Ding [a, *]

[a] Energy & Environmental Science and Technology, Idaho National Laboratory, Idaho Falls, ID 83401, USA
[b] School of Industrial Engineering, Purdue University, West Lafayette, IN 47907, USA
[c] Department of Mechanical Engineering, The University of Maine, Orono, ME 04469, USA

ARTICLE INFO

Keywords:
Propane dehydrogenation
Propylene production
Protonic SOFC
PtGa catalyst
Energy conversion

ABSTRACT

Protonic solid oxide fuel cells (p-SOFC) integrated with clean thermal energy sources are promising platforms for decarbonized chemical production in addition to power generation, such as on-purpose propylene production from propane dehydrogenation (PDH). The catalytic performance of the conventional nickel-cermet-based anode materials in p-SOFC for propane conversion is restrained by their low active surface area and proneness to coking. In this work, by integration of a highly efficient industry-relevant thermal catalyst PtGa/ZSM-5 for PDH reaction, we demonstrate that both the electrochemical and catalytic performance of the propane-fueled p-SOFC can be effectively enhanced. The PtGa catalyst integrated p-SOFC exhibits a peak power density of 93 mW cm^{-2} at 600 °C, which is greater by about 100% and 50% than that without catalyst or with a perovskite-based $(Pr_{0.3}Sr_{0.7})_{0.9}Ni_{0.1}Ti_{0.9}O_3$ (PSNT) catalyst layer, respectively. The PDH activity and olefin selectivity of the PtGa catalyst is also significantly higher than that of the PSNT catalyst. In addition, much improved coke tolerance and propylene selectivity (over 90%) compared to the catalyst-free Ni-cermet anode materials were achieved by integrating the industrial catalyst layer. The propane conversion can be further improved by an applied current density, whereas the olefin selectivity is almost unaltered. The excellent performance of the PtGa catalyst integrated p-SOFC is attributed to the high surface area, intrinsically high catalytic activity, selectivity, and anti-coking properties of the catalytic layer for propane conversion. This work provides a general approach and a case study for boosting the performances of p-SOFCs in chemical production by integrating thermo- and electro- catalysis.

1. Introduction

Propylene is one of the most important platform chemicals for manufacturing various value added chemical and polymeric products [1–3]. Conventionally, propylene is obtained mainly as a coproduct with ethylene from steam cracking of crude oil in petroleum refining processes, which is highly energy intensive and significantly contributes to CO_2 and NO_x emissions [2,3]. In recent years, with the shift to ethane cracking as a source for ethylene, which produces no propylene, on-purpose/distributed technologies are being sought increasingly for propylene production to meet the rising demand throughout the world [1]. Non-oxidative catalytic propane dehydrogenation (PDH), usually operated at around 600–650 °C, is the primary on-purpose technology in use nowadays [4,5]. This approach, however, has drawbacks including relatively high energy demand, low single-pass conversion limited by the thermodynamic equilibrium, and rapid coking-induced deactivation of the catalysts [4,5].

To address the issues with the PDH technology, electrochemical membrane reactors based on proton-conducting solid oxide fuel cells (p-SOFC) have been explored as a novel promising approach for propylene production from propane [6–13]. By conducting PDH reaction in the p-SOFC, the hydrogen byproduct from the dehydrogenation reaction can be effectively separated from the product stream through the proton-conducting electrolyte membranes in the form of protons. As a result, the thermodynamic limitation could be overcome and thus the single pass propane conversion is no longer equilibrium limited [13]. In

* Corresponding authors.
E-mail addresses: lucun.wang@inl.gov (L.-C. Wang), wu966@purdue.edu (W. Wu), dong.ding@inl.gov (D. Ding).
[1] Equal contribution.

https://doi.org/10.1016/j.fuel.2023.129685
Received 5 July 2023; Received in revised form 16 August 2023; Accepted 30 August 2023
0016-2361/© 20XX

addition, electric power can be generated via the recombination of the protons and oxygen on the other side of the cell. Compared with the conventional hydrocarbon fueled oxygen-ion-conducting SOFC (o-SOFC) [14–16], there are essentially no CO_2 emissions in the power generation process in p-SOFCs.

The lower operating temperatures of the p-SOFC relative to the o-SOFC [11,12,17] bring about benefits to the structural stability of the cell components as well as reduced energy consumption of the reactor system. Nevertheless, lower temperatures also result in significantly suppressed kinetics of PDH reaction, which necessitates the development of highly active catalysts to compensate the loss in the yield of olefin products. To date, efficient conversion of alkane to light olefins in p-SOFCs mainly suffer from low power densities, severe coke deposition, and complex side reactions on the anodes [12,18–21]. These drawbacks can be attributed in part to the use of Ni-based anodes, which have excessive catalytic activity toward hydrocarbon cracking reactions [4,22]. Stable and efficient cogeneration of electricity and light olefins have recently been achieved by using a novel Pr and Ni co-doped $SrTiO_3$ perovskite catalyst with A-site deficiency [19]. Although good operating stability was achieved in propane fuels, the conversion and selectivity of propylene at 600 °C was only ~ 6% and ~ 27%, respectively [19]. The performances of perovskite-structured electrocatalysts are usually severely limited by their low surface areas, which result from the typically harsh (≥1000 °C) sintering/firing conditions during catalyst synthesis and cell fabrication processes [18–21]. In contrast, the catalysts commonly used in thermal catalytic PDH reaction are supported on high-surface-area materials, such as silica, alumina, and zeolites, to maximize the number of active sites on the surface [5]. The direct use of thermal catalysts in SOFC systems, however, has been usually considered impractical, mainly due to their low electrical conductivities [23–26] thus being incompatible with the electrochemical environment.

In this work, we demonstrate that high-surface-area heterogeneous catalysts for thermal catalytic PDH reaction can be directly incorporated with p-SOFC, serving as a highly efficient electrocatalytic membrane reactor system for cogeneration of propylene and electric power with both boosted catalytic activity and high electrochemical performance. A highly active bimetallic PtGa catalyst supported on ZSM-5 type zeolite was employed for propane conversion. The catalyst-loaded p-SOFC single cell exhibited a good and stable electrochemical performance. Much improved carbon tolerance and propylene selectivity (over 90%) was obtained with the incorporated catalyst layer on the p-SOFC. Our work provides a general and facile approach to integrate the state-of-the-art industry-relevant catalysts directly on the SOFC to co-generate electricity and various chemicals through different chemical reactions.

2. Experimental

2.1. Catalyst synthesis

The PtGa/ZSM-5 bimetallic catalysts were synthesized by the incipient wetness impregnation method using ZSM-5 (CBV 5524G, Si/Al = 25, surface area 425 m²/g, Zeolyst International) as the support. Tetraammineplatinum nitrate $Pt(NH_3)_4(NO_3)_2$ (99.9%, Alpha Aesar) and gallium nitrate $Ga(NO_2)_3{\cdot}8H_2O$ (99.999%, Alpha Aesar) were mixed in an aqueous solution and then added dropwise to ZSM-5 so that the solutions can fill the pores of the ZSM-5 support. The nominal loading of Pt and Ga is 3 wt%. The mixture was dried in an oven overnight at 100 °C, then calcined in dry air at 400 °C for 1 h, and finally reduced by 20% H_2/Ar at 700 °C for 1 h. The catalysts were further annealed at 400 °C for 2 h under same flow to enhance alloying.

For comparison, the $(Pr_{0.3}Sr_{0.7})_{0.9}Ni_{0.1}Ti_{0.9}O_3$ (PSNT) catalyst with A-site deficiency were prepared using a glycine and citric acid assisted combustion method similar to that reported previously [19]. Briefly, stoichiometric amounts of titanium(IV) isopropoxide $C_{12}H_{28}O_4Ti$ (97%, Sigma Aldrich), strontium nitrate $Sr(NO_3)_2$ (99.995%, Sigma Aldrich), praseodymium(III) nitrate (99.9%, $Pr(NO_3)_3{\cdot}6H_2O$, Alfa Aesar), and nickel nitrate (99 + %, $Ni(NO_3)_2{\cdot}6H_2O$, Alfa Aesar) were dissolved in deionized water under continuous stirring. Then glycine and citric acid were added as the complexing agents at a molar ratio of metal/glycine/citric acid = 1/2/2. The solution was heated under stirring until self-ignition occurred. The as-obtained powders were calcined at 1000 °C for 2 h to form the perovskite phase structure.

2.2. Powder synthesis for cell fabrication

The $BaCe_{0.7}Zr_{0.1}Y_{0.1}Yb_{0.1}O_{3-\delta}$ (BCZYYb) powders used for the electrolyte and anode were prepared by the solid-state reaction method using stoichiometric amount of precursors including barium carbonate (Sigma Aldrich, 99%, $BaCO_3$), zirconium oxide (Alfa Aesar, 99%, ZrO_2), cerium (IV) oxide (Aldrich, 99.9%, CeO_2), yttrium (III) oxide (Alfa Aesar, 99.99%, Y_2O_3), and ytterbium (III) oxide (Alfa Aesar, 99.9%, Yb_2O_3). The powder was ball milled for 24 h in ethanol, dried for 24 h, crushed, and calcined at 1100 °C for 10 h. The process was repeated to form a pure perovskite phase. The $PrNi_{0.5}Co_{0.5}O_{3-\delta}$ (PNC) cathode material was synthesized by a modified glycine-citrate combustion method, where nitric acid and glycine were used as parallel complexing agents [27]. The precursor solution was prepared by dissolving stoichiometric amounts of $Pr(NO_3)_3{\cdot}6H_2O$ (99.9%, Alfa Aesar), $Ni(NO_3)_3{\cdot}6H_2O$ (99 + %, Alfa Aesar), and $Co(NO_3)_3{\cdot}6H_2O$ (99%, STREM Chemicals) in a citrate-glycine aqueous solution. Under heating and stirring conditions, the viscous gel was ignited to obtain the ash that was further calcined at 1000 °C in air for 5 h to form the perovskite structure.

2.3. Characterizations

The morphology and the elemental distribution at the cross-section of the cells were characterized by field emission scanning electronic microscopy (SEM JEOL 6700F) combined with energy dispersive X-ray spectroscopy (EDS) analysis. The microstructure and elemental mapping of the catalyst nanoparticles were confirmed by the scanning transmission electron microscopy (STEM, FEI Tecnai F30) equipped with EDS. The structure of the catalysts was also examined by the X-ray powder diffraction analysis (XRD, D8ADVANCE/Germany Bruker) with the 2θ ranging from 20° to 80° at a scanning step of 0.02° min⁻¹. The temperature programmed reduction with H_2 (H_2-TPR) experiments were performed using the OmniStar gas analysis system (GSD 320 O1). 100 mg of each sample was pretreated at 120 °C for 30 min in a gas flow (50 mL min⁻¹) of argon, followed by cooling down to room temperature. The reduction was conducted in 10% H_2/Ar (20 mL min⁻¹) by heating the sample from room temperature to 600 °C at 10 °C min⁻¹ while recording the MS signals of H_2 (m/z = 2) and H_2O (m/z = 18).

2.4. Electrochemical cell fabrication

Button cells with a configuration of NiO-BCZYYb|BCZYYb|PNC were fabricated by a standard procedure. Briefly, a mixture of NiO (Alfa Aesar) and BCZYYb powder (a weight ratio of 60:40) was mixed in ethanol and toluene using a high-energy ball mill (SPEX, 8000 M) for 20 min. Plasticizers and binders were added and then mixed for another 20 min to obtain a slurry, which was degassed and tape-cast to form green tapes. After drying overnight, the green tape was punched into 5/16 in., followed by pre-firing at 950 °C for 2 h forming anode supports (~0.3 mm thick). Then, a thin layer of BCZYYb (~10 μm) was deposited on the anode support by a slurry coating process followed by co-firing at 1400 °C for 4 h. Subsequently, the PNC ink was screen printed onto the top of the BCZYYb electrolyte and fired at 900 °C for 2 h to form a porous cathode. The active electrode area for all cells is 0.0176 cm². To incorporate the catalyst layer, a slurry containing 20 wt% PtGa/ZSM-5 or PSNT, 40 wt% 441-thinner, and 40% ethanol was first prepared and then brush painted on the Ni-BCZYYb anode, followed by drying at 80 °C for 1 h.

2.5. Catalyst and cell performance test

The electrochemical cell was fixed in a home-made reactor (Fig. S1). Silver mesh and silver wire were used as the current collector and leads, respectively. A thermal couple was placed in the reactor to monitor the cell temperature. The cell temperature was ramped to 650 °C under a flow of air (30 mL min^{-1}) and stabilized for 30 min. Then pure H_2 with a flow rate of 10 mL min^{-1} was introduced at the NiO-BCZYYb electrode to reduce NiO to Ni. After reduction, the temperature was lowered to 550 °C for the subsequent performance test. At each testing temperature, a sweeping gas of argon was first introduced to the anode to flush out residual H_2, and then the propane gas mixture ($C_3H_8/H_2/Ar/$ = 5/5/40, total flow rate 50 mL min^{-1}) was used as the feed gas. In the cathode, air was used as the sweeping gas. The measurements were carried out in the frequency range from 0.1 Hz to 1 MHz with a bias voltage of 10 mV. To evaluate the electrochemical performance of the cells, potential-current (I-V) curve and the electrochemical impedance spectroscopy (EIS) were recorded using a Solartron 1400 electrochemical working station after a stable open circuit voltage (OCV) was reached. The catalytic activity and selectivity were also measured under both OCV and different discharging or applied current density conditions by using a gas chromatography (GC, Shimadzu 2010 plus) to analyze the gas compositions at the exit of the anode side. The conversion of propane (X_{C3H8}) and olefin selectivity (S) were determined by the following equations:

$$X_{C3H8}\,(\%) = \frac{[F_{C3H8}]_{in} - [F_{C3H8}]_{out}}{[F_{C3H8}]_{in}} \times 100$$

$$S\,(\%) = \frac{n_{C2H4} \times [F_{C2H4}]_{out} + n_{C3H6} \times [F_{C3H6}]_{out}}{\sum n_i [F_i]_{out}} \times 100$$

Where i represents the hydrocarbon product in the effluent gas (excluding propane), n_i is the number of carbon atoms of component i, and $[F_i]$ is the corresponding molar concentration.

3. Results and discussion

3.1. Characterization of catalysts

The XRD patterns of as-prepared and used PtGa/ZSM-5 catalyst (Fig. S2) showed the typical diffraction features of MFI-type structure. No diffraction peaks characteristic of metallic Pt or PtGa alloy phases can be identified before or after reaction, which may be accounted for by the presence of highly dispersed Pt or PtGa species or very low loading amount of Pt and Ga. Fig. S3a shows the high-angle annular dark field STEM image of the PtGa/ZSM-5 catalyst after reduction pretreatment at 700 °C. The bright spots dispersed on the zeolite matrix correspond to the PtGa alloy particles, which exhibit a relatively wide distribution of the particle size ranging from sub-nanometer to around 20 nm. The formation of alloy structure between Pt and Ga is evidenced by the elemental mapping results in Fig. S3b and S3c, which clearly shows the overlapping distribution of these two elements in almost all detectable nanoparticles. The co-existence of Pt and Ga in the nanoparticles is further confirmed by the EDS result shown in Fig. S3d. The STEM-EDS results of the PtGa catalyst after reaction (Fig. S4) showed that the PtGa nanoparticle sizes increased to some extent and appeared to become more homogenous in distribution.

The reduction properties of Pt and Ga species in the catalyst upon the pretreatment is investigated by the H_2-TPR experiment. The reduction profile of the PtGa/ZSM-5 catalyst in Fig. S5 shows that there are three major reduction peaks at ca. 242, 384, and 640 °C. To understand the reduction process associated with each peak, TPR experiment was also performed for the monometallic catalysts, namely, Pt/ZSM-5 and Ga/ZSM-5. Comparing the reduction profiles of these three catalysts reveals that the first two low-temperature peaks should originate from the reduction of both Pt and Ga oxides in close proximity, whereas the high temperature peak at 640 °C may be attributed to the reduction of segregated Ga oxide particles in strong interaction with the zeolite support [28].

The crystallite structure of the reference catalyst PSNT was characterized by XRD. The characteristic diffraction peaks in Fig. S6 clearly indicate the formation of a cubic perovskite phase with *Pm*3*m* (2 2 1) space group (JCPDS card no. 35–0734). A reduction treatment in H_2 at 1000 °C for 2 h resulted in no substantial changes to the peak position except for an increase in the peak intensity. In addition, a small new peak emerged at 2θ = 44.3°, corresponding to the (1 1 1) diffraction of metallic Ni phase, suggesting the exsolution of Ni^0 nanoparticles from the bulk structure of PSNT. The occurrence of Ni exsolution was further confirmed by the SEM characterization of PSNT before and after reduction (Fig. S7), which clearly shows that a large amount of Ni nanoparticles with a homogenous size of about 10–20 nm was generated on the reduced PSNT surface, in stark contrast to that before reduction treatment. In addition, the almost identical XRD pattern of PSNT after reaction to that of the reduced PSNT suggests that there were negligible further changes in the bulk structure under reaction conditions.

3.2. Catalytic performance in PDH reaction

The catalytic performances of both PtGa/ZSM-5 and PSNT catalysts in PDH reaction were first evaluated in a fixed-bed flow reactor at different temperatures. The propane conversion on PtGa/ZSM-5 catalyst was 33.1%, 37.5%, and 45.4% at 550, 600, and 650 °C, respectively (Fig. 1a). In contrast, the PSNT catalyst exhibited significantly lower activity by a factor of 2 ~ 3 under the same reaction conditions, with the corresponding propane conversion of only 10.8%, 13.0%, and 19.6%. As far as the selectivity is concerned, the olefin product selectivity appears to be relatively higher on PSNT than that on PtGa/ZSM-5 catalyst, especially at higher temperatures (Fig. 1b). It should be pointed out, however, that a reasonable direct comparison of selectivity should be made at a comparable conversion level. Based on the propane conversion at different temperatures, the apparent activation energies (E_a) of PDH reaction over different catalysts can be estimated from the Arrhenius plots (Fig. S8), namely, 19.8 kJ mol^{-1} for PtGa/ZSM-5 and 37.4 kJ mol^{-1} for PSNT. Apparently, the relatively lower E_a on PtGa/ZSM-5 catalyst should be at least partly responsible for its superior catalytic performance to that on PSNT catalyst. In addition, the greater value of the intercept in the Arrhenius plot for PtGa/ZSM-5 catalyst also indicates a higher number of surface active sites than that on the PSNT catalyst (Fig. S8). Along this line, the distinctly different textural properties of the two types of catalysts should also be taken into account. The N_2 physisorption on the PtGa/ZSM-5 catalyst shows a type I adsorption isotherm and a H4 type hysteresis loop, typical for microporous materials (Fig. S9). The quantity of adsorbed nitrogen slightly decreased after reaction, probably due to a partial blockage of the pore structures by coke formation. The corresponding BET surface area of the fresh and used PtGa catalyst was measured to be 370 and 355 cm^2/g, respectively. In contrast, the N_2 sorption isotherm of the PSNT catalyst shows a significantly lower quantity of adsorbed nitrogen with a BET surface area of 14.6 cm^2/g.

The reusability of the PtGa/ZSM-5 catalyst for PDH reaction was also investigated. A batch of fresh catalyst was first subjected to reaction at 600 °C using a H_2-free propane feed gas to induce more severe deactivation by coking. After reaction for 20 h, the catalyst activity declined by over 80%, while the propylene selectivity remained constant at around 75% (Fig. S10). The catalyst was subsequently exposed to air at the same temperature for 1 h and then back to the reaction condi-

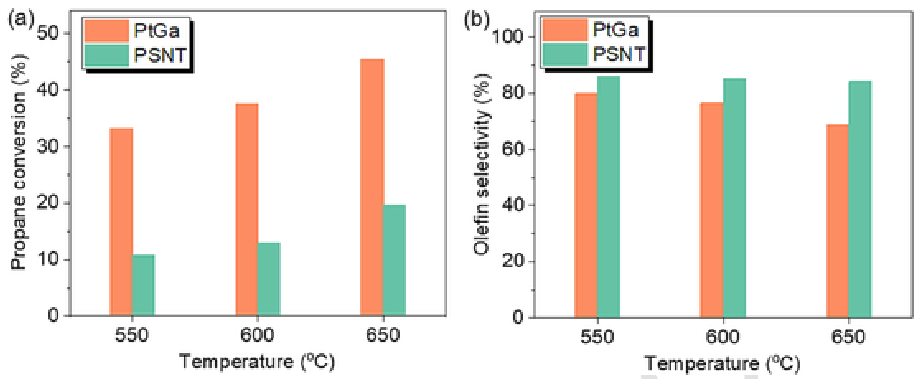

Fig. 1. Comparison of the catalytic performance between PtGa/ZSM-5 and PSNT catalysts measured in a fixed bed flow reactor at different temperatures: (a) propane conversion and (b) olefin (propylene and ethylene) selectivity. Reaction conditions: 100 mg catalyst, $C_3H_8/H_2/Ar$ = 5/5/40, total flow rate 50 mL min⁻¹.

tions. The results showed that not only the initial propane conversion and propylene selectivity were almost completely restored, the evolution trend of the catalytic performance with time also remained the same. Clearly, the performance degradation of the PtGa/ZSM-5 catalyst is fully reversible, consistent with the presumption that the degradation was primarily caused by coke formation.

3.3. Characterization of p-SOFC with integrated catalyst

A schematic drawing of the configuration of the p-SOFC electrochemical membrane reactor with the electrode reactions is illustrated in Fig. 2a. The representative SEM images of the cross section of the cell before and after testing are shown in Fig. 2b and S11, respectively. The cell consists of a thin BZCYYb electrolyte (~15 µm), the NiO-BZCYYb anode support (~450 µm) with a PtGa/ZSM-5 catalyst layer (~50 µm),

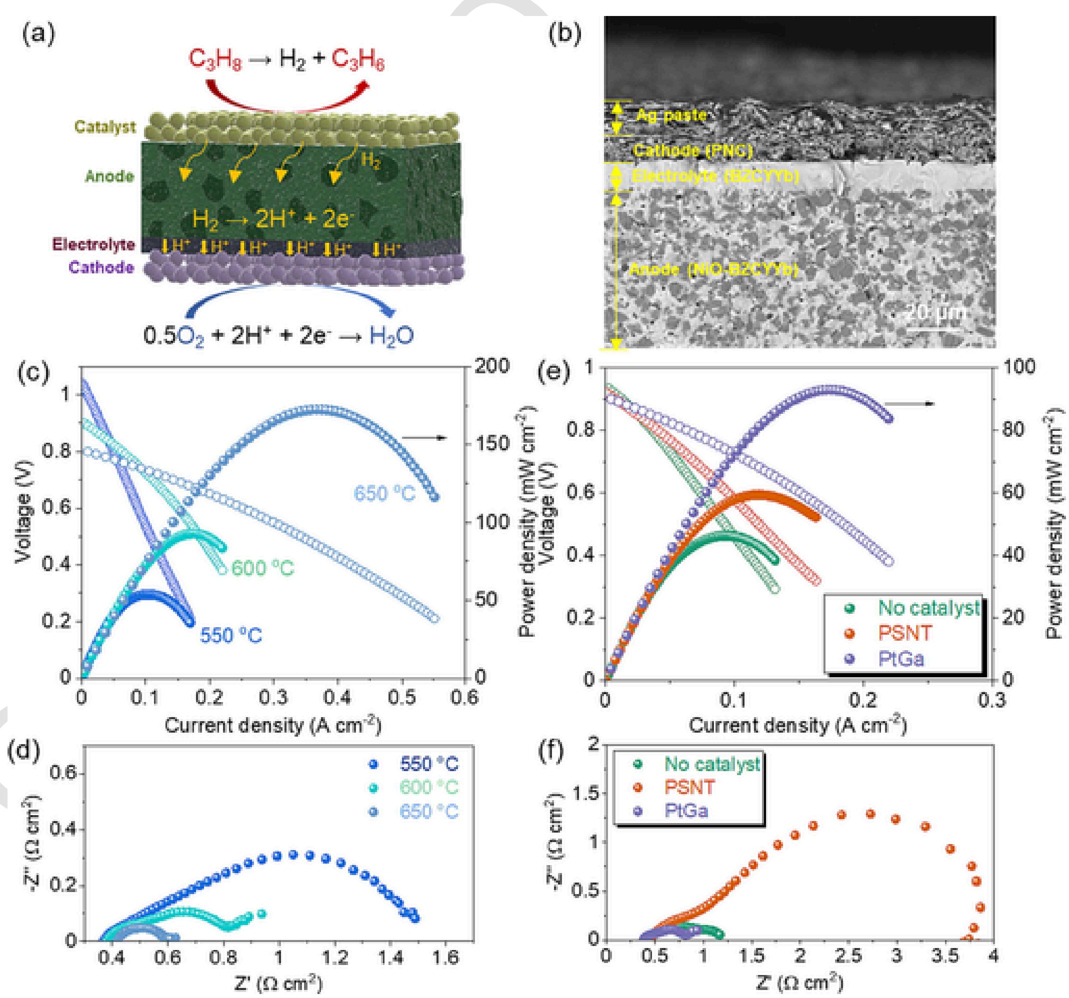

Fig. 2. (a) Schematic of catalyst-integrated propane-fueled p-SOFC. (b) SEM image of the cross section of the electrode-supported cell before test. (c) Polarization curves and (d) impedance spectra of the catalyst-integrated p-SOFC using propane as the fuel between 550 and 650 °C. (e) Polarization curves and (f) impedance spectra. of p-SOFC with or without the catalyst layer using propane as the fuel at 600 °C.

and a three-dimensional mesh-like PNC cathode (~10 μm). In a typical propane-fueled SOFC process, propane is fed to the catalyst-incorporated anode and dehydrogenated to propylene, electrons, and protons. Under an applied potential or discharging current, the protons are immediately transported through the electrolyte and recombine with electrons and oxygen at the cathode side to produce H_2O.

The acceptor-doped barium zirconate cerate BCZYYb exhibits high ionic conductivity and hydrogen permeability at intermediate temperatures (400 – 700 °C), which is an ideal electrolyte material for the nonoxidative PDH reaction. It should be noted that the conducting behavior of BZC-based material is highly temperature sensitive. At elevated temperatures above 700 °C, this type of materials can exhibit both proton and oxide ion conductivity [29]. As a result, it becomes highly likely that propane may undergo oxidation reactions to produce carbon oxides, leading to reduced selectivity of olefin products including propylene and ethylene. Accordingly, to minimize the contribution of oxidation-induced propane conversion, the operation temperature for the performance test experiments in this work was set below 700 °C, namely, in the range of 550 – 650 °C. Considering the stable and high electrochemical performance in both electrolysis and fuel cell modes, the triple-conducting ($H^+/O^{2-}/e^-$) PNC was employed as the cathode material [27]. Incorporation of the three-dimensional mesh-like PNC electrode can continuously extract the produced hydrogen from the anode side and break the thermodynamic limitation for propane conversion.

3.4. Performance evaluation of p-SOFC with integrated catalyst

The electrochemical performance of the p-SOFC was initially evaluated using H_2 as the fuel. The temperature-dependent potential and power density plots as a function of current densities in H_2 are presented in Fig. S12a, and the corresponding EIS results are shown in Fig. S12b. An OCV of 1.07, 1.05 and 1.03 V was obtained at 550, 600, and 650 °C, respectively. The measured OCVs are quite close to the thermodynamic reversible potentials, which indicates that the electrolyte is dense, and the cell is sealed well. As the temperature increases from 550 °C to 600 and 650 °C, the peak power density (PPD) increases from 173 mW cm^{-2} to 369 and 512 mW cm^{-2}, respectively. According to the EIS data (also see Table S1), the ohmic loss (R_o) of the cell due to the resistance of ionic and electronic conduction, determined from the high frequency intercepts of the spectra with the real axis, is 0.47, 0.35, and 0.30 Ω cm^2 at 550, 600, and 650 °C, respectively, and the corresponding polarization resistance (R_p) is 0.59, 0.20, and 0.08 Ω cm^2.

When the fuel gas was switched from pure H_2 to propane gas mixture, the PPD at each temperature (Fig. 2c) decreased to different extents to 54, 93, and 172 mW cm^{-2} at 550, 600, and 650 °C, respectively. The lower PPD in propane is attributed to the relatively slower activation kinetics of propane compared with that of H_2 on the catalyst-loaded Ni-BCZYYb anode. Note that the OCVs for the propane-fueled cell are relatively lower than those for the cell fed with hydrogen. This can be rationalized by comparing the theoretical OCVs for both fuel cell reactions. The overall reaction in the propane-fueled p-SOFC can be represented by the oxidative propane dehydrogenation (OPDH, $C_3H_8 + 0.5O_2 \rightarrow C_3H_6 + H_2O$). Based on the Nernst equation, the theoretical OCV (E) at different temperatures can be calculated from the Gibbs free energy (ΔG) of this reaction under thermodynamic equilibrium conditions using the following equation: $\Delta G = -nFE$. The calculated values of ΔG and the corresponding E as a function of temperature (Fig. S13) indicate that the OCVs for OPDH are lower than those for hydrogen oxidation in the temperature range of 300–900 °C. In addition, the theoretical OCVs for both reactions decrease with temperature. These results agree well with the trend obtained from our experimental results as well as that reported in the literature [19].

According to the EIS results (Fig. 2d and Table S1), the ohmic resistance is comparable in H_2 and propane at the same temperature, while the polarization resistance in propane is obviously greater than that in H_2. For example, at 600 °C, the R_o values in propane and H_2 are 0.38 Ω cm^2 and 0.35 Ω cm^2, respectively, while the R_p values in propane and H_2 are 0.44 Ω cm^2 and 0.20 Ω cm^2, respectively. The relatively higher R_p in propane is consistent with the lower PPD and again reflects the more sluggish reaction kinetics of propane as compared with that for hydrogen, especially at lower temperatures. In fact, similar results have been reported previously for p-SOFCs using light alkanes as the fuel including both ethane and propane [12,18–21].

To assess the effect of PtGa catalyst layer on the performance of the p-SOFC, a Ni-BCZYYb|BCZYYb|PNC single cell was fabricated without incorporating the catalyst layer on the Ni-BCZYYb electrode. In addition, another cell with the PSNT catalyst layer was also fabricated for comparison. The electrochemical performance in terms of polarization curve and impedance of these two cells was evaluated under the same reaction conditions and compared with that of the PtGa catalyst-loaded cell. As shown in Fig. 2e, a PPD of 46 mW cm^{-2} was obtained on the catalyst-free cell at 600 °C. In the presence of the PSNT catalyst layer, the PPD increased to 60 mW cm^{-2}. In contrast, the PPD was 93 mW cm^{-2} with the PtGa catalyst layer on the anode, which is greater by 100% and 53.3% relative to the catalyst-free and PSNT catalyst-loaded cells, respectively. In accordance with the polarization curves, the incorporation of the PtGa catalyst layer also led to a decrease in the R_o and R_p to different extents (Fig. 2f) compared to that without catalyst (see Table S1). Note that the PSNT-loaded cell exhibited a significantly greater R_p especially in the low-frequency region, pointing to severe limitations in mass transfer during the electrochemical conversion of propane. Similar EIS spectrum has been reported previously for the PSNT catalyst [19]. This may be attributed to the rather low surface area and pore volume of the PSNT catalyst (0.011 cm^3 g^{-1} for PSNT vs. 0.087 cm^3 g^{-1} for PtGa/ZSM-5) resulting from the high sintering temperature (1000 °C) as compared with the PtGa/ZSM-5 catalyst.

The catalytic performance in PDH reaction was also measured for the cells with different catalyst layers as well as that without the catalyst layer. In the absence of catalyst layer, the propane conversion on the Ni-BCZYYb electrode was only 4.7% with the olefin selectivity of 11.8% (Fig. 3a) at 550 °C. This result is consistent with the fact that Ni metal is a poor catalyst for selective dehydrogenation reaction of light alkanes due to its a high intrinsic activity toward C–C bond cleavage, leading to the formation of methane and carbon deposits [22]. Adding the PSNT catalyst layer resulted in higher propane conversion of 7.3% and a dramatically improved olefin selectivity of 89.2%. In the presence of the PtGa/ZSM-5 catalyst layer, a further increase in the propane conversion and olefin selectivity to 14.7% and 94.1%, respectively, was obtained. Note that the propane conversions obtained here are significantly lower than that from the fixed bed flow reactor experiments described above (see Fig. 1), especially for the PtGa catalyst. This discrepancy is simply due to the much less amount of loaded catalyst given the limited space on the cell. In specific, the actual amount of PtGa/ZSM-5 catalyst in the thin catalyst layer on the p-SOFC is only about 25 mg, whereas the amount of PSNT is about 80 mg.

Both the electrochemical and catalytic performances of the PtGa catalyst integrated p-SOFC are further compared with those reported in the literature (Table S2). Note that the number of previous studies on propane-fueled p-SOFC is rather limited [19,30,31]. Therefore, those works on propane-fueled o-SOFC are also included for comparison [32–37]. Clearly, both the PPD and olefin yield obtained in this work are distinctly higher than that reported in previous works under even lower temperature conditions (by at least 50 °C), demonstrating the great potential of p-SOFC in propane conversion when integrated with highly active and selective thermal catalysts.

The stability of the catalytic performance of the p-SOFC with the PtGa catalyst layer was also investigated. The propane conversion underwent a relatively fast decrease in the first two hours of reaction, followed by a slow decay for over 10 h (Fig. 3b). A similar trend was ob-

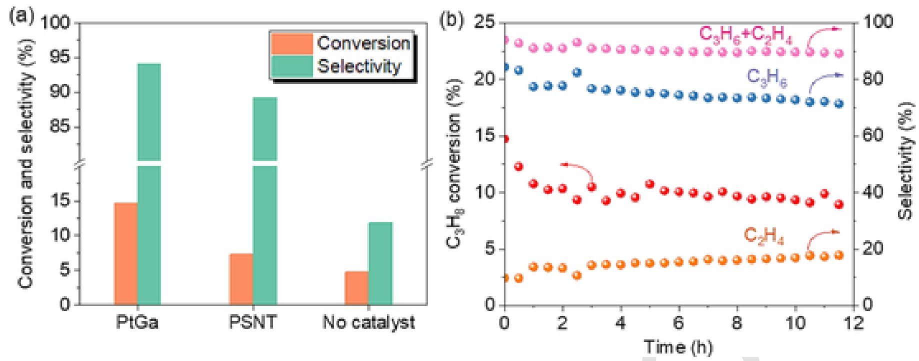

Fig. 3. Catalytic performance of p-SOFC with or without the catalyst layer in PDH reaction at 600 °C: (a) conversion and selectivity with different catalyst layers and without catalyst, (b) short-term stability of the catalytic performance with the PtGa catalyst layer.

served for propylene selectivity. In contrast, there was a moderate and steady increase in the selectivity of the other olefin product, ethylene. As a result, the overall olefin selectivity remained almost constant throughout the short-term test.

3.5. Effect of current density on the performance of p-SOFC with integrated catalyst

To investigate the electrochemical effect on the catalytic performance of the catalyst layer, the cell was first operated in fuel cell mode at different output current densities of 40, 80, and 120 mA cm^{-2} at 600 °C. The propane conversion and product selectivity at each current density were measured three times, the average values of which are reported in Fig. 4. The results showed that the propane conversion declined continuously from 14.1% to 13.0% as the current density increases from 40 mA cm^{-2} to 120 mA cm^{-2}, whereas the selectivity of different products including methane, ethylene, and propylene is essentially unaltered upon the variation of current densities. At first glance, these results seem to be in stark contrast to that recently reported in a similar study using the PSNT catalyst for a propane-fueled p-SOFC [19], where the current density was found to have a negligible effect on the propane conversion but promotional effect on the selectivity of both ethylene and propylene products. Nevertheless, we suspected that the thermal deactivation of the catalyst as shown in Fig. 3b may also contribute to the declining propane conversion as the current density increases. To verify this possibility, the catalyst performance was measured again under OCV conditions following the experiment at different current densities. The re-measured propane conversion became 12.8% (Fig. 4a), essentially the same as that at 120 mA cm^{-2} within the experimental error, whereas the initial conversion at OCV was 14.4%. Apparently, the output current density in the fuel cell mode should have little effect on the propane dehydrogenation reaction, in good agreement with the literature results.

As far as the selectivity is concerned, it has been reported that the propylene selectivity increased from 31.8 % at OCV to 36.3 % at 300 mA cm^{-2} with the ethylene selectivity increasing from 28.5% to 32% [19]. It should be pointed out, however, that the dependence of olefin selectivity on the current density in the previous work is not straightforward. In fact, a closer inspection of the reported data revealed that there was even a slight decrease in the selectivity of both ethylene and propylene as the current density increased from 100 to 200 mA cm^{-2} [19]. In addition, the magnitude of increase in selectivity as a function of the current density is rather limited especially when the possible experimental errors are taken into account. Nonetheless, the seemingly different effect of current density on olefin product selectivity obtained in this work may be related to the different reaction conditions including temperature (600 °C in this work vs. 700 °C in the literature [19]) and the composition of the feed gas (no water vs. 10% water in the feed gas [19]). It is likely that the relatively lower reaction temperature renders the electrochemical effect on the thermal catalytic reactions even less significant for experimental verification.

The electrochemical effect on the catalytic performance of the catalyst layer was also investigated by imposing an overpotential on the cell at different applied current densities from −100 mA cm^{-2} to −400 mA cm^{-2} when the relatively steady state was reached during the PDH reaction. The corresponding propane conversion and selectivity as a function of different applied current density are presented in Fig. 5a and 5b, respectively. The propane conversion increased from 8.5% under OCV conditions to 10.3% when a current density of −100 mA cm^{-2} was applied. Upon further increase in the applied current density, there was a steady increase in the propane conversion, which appears to level off at higher applied current densities. In contrast, the product selectivity seems less affected by the applied current density. The selectivity of

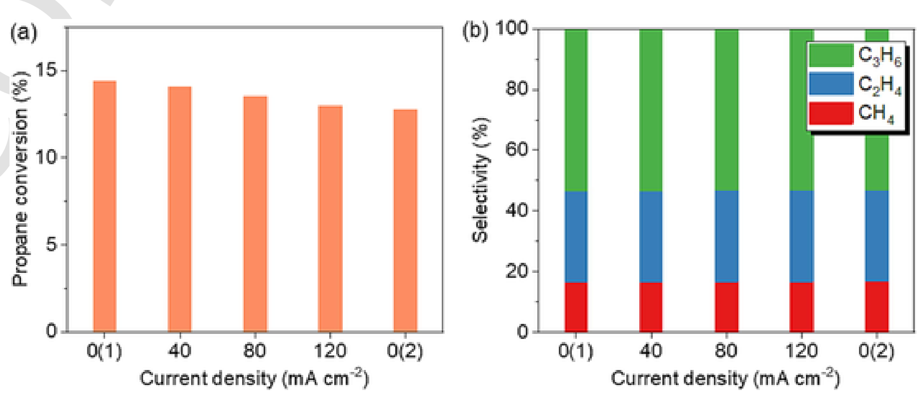

Fig. 4. The effect of current density on the catalytic performance of p-SOFC with PtGa catalyst layers in propane dehydrogenation reaction at 600 °C: (a) propane conversion and (b) selectivity.

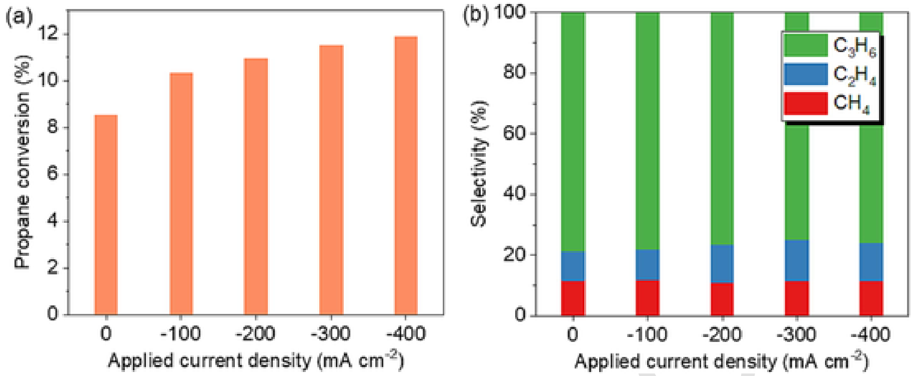

Fig. 5. The effect of applied current density on the catalytic performance of p-SOFC with PtGa catalyst layers in propane dehydrogenation reaction ($C_3H_8/H_2/Ar/ = 5/5/40$, total flow rate 50 mL min^{-1}, 600 °C): (a) conversion and (b) selectivity.

the major byproduct methane hardly changed as the current density increases, whereas there was a slight increase in the ethylene selectivity at the expense of propylene, from 10% at −100 mA cm^{-2} to 13% at −400 mA cm^{-2}. Similar experiments were also performed on the PSNT-loaded cell and the overall trend is almost the same as that observed on the cell with the PtGa catalyst layer, except for the relatively lower propane conversion and propylene selectivity (see Fig. S14).

The enhanced propane conversion may originate, at least in part, from the electrochemical activation of propane, namely, the electrochemical promotion of the catalytic propane dehydrogenation reaction [38,39]. While such an effect cannot be ruled out for the PSNT catalyst given its high conductivity according to recent reports [19], this effect is less likely for the PtGa/ZSM-5 catalyst in view of the low electronic conductivity of the zeolite supporting materials [25,26]. Instead of direct electrochemical propane activation, the promotional effect of the applied current density on the propane conversion over PtGa catalyst-loaded cell may result directly from the shift of reaction equilibrium to the right direction due to the enhanced proton transfer from the anode to the cathode side under the applied current density. We propose a tandem reaction mechanism involving thermal catalytic propane dehydrogenation on the PtGa catalyst layer followed by electrochemical activation of hydrogen on the Ni electrode to form protons (see schematic in Fig. 2a). It is reasonable to speculate that both the formation of protons and their ensuing transfer through the electrolyte membrane could be accelerated by the externally applied current density.

The electrochemical performance stability of the p-SOFC with the catalyst layer under an applied current density was further investigated. The corresponding voltage was recorded as a function of time at a constant current density of −200 mA cm^{-2} at 600 °C. The results (Fig. 6a) show that the voltage steadily decreases from about 1.11 V to 0.73 V after operation for 20 h. The stability test was also conducted on the catalyst free p-SOFC and the results are included in Fig. 6b for comparison. As expected, there is a rapid degradation in the cell voltage in several minutes of reaction due to severe carbon deposition, consistent with that reported in the previous study [19]. The decrease in voltage over the catalyst loaded cell may be associated with the OCV drop during the PDH reaction, which occurs in parallel to the carbon deposition on the anode. The OCV loss may also stem from the non-negligible current leakage that is known to occur in thin-layer barium-zirconate-cerate-based proton conductors under fuel cell operating conditions at > 600 °C [40–42]. To check whether electronic leakage is responsible for the voltage decrease, the impedance spectrum was collected after the 20-h test and compared with that before the test. In principle, a notable decrease in the ohmic resistance could be measured if electronic leakage occurs. Nevertheless, the EIS data (Fig. 6c) indicates that there was negligible change in the ohmic resistance. In contrast, a substantial increase in the polarization resistance took place, which is most likely caused by the carbon deposition. Obviously, the distinctly different stability under the same applied current density in the presence or absence of the PtGa catalyst layer should primarily originate from the different anti-coking properties rather than the electronic leakage. Moreover, it is interesting to note that the trend of voltage decrease closely resembles that of the decay in propane conversion as shown in Fig. 3b, presumably pointing to a common mechanism for both electrochemical and catalytic performance degradation.

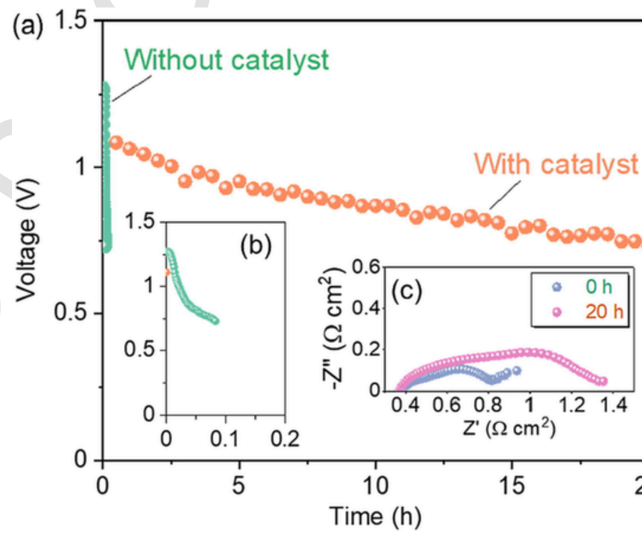

Fig. 6. (a) Shor-term stability of the electrochemical performance of propane-fueled p-SOFC with or without the PtGa catalyst layer under applied current density of −200 mA cm^{-2} at 600 °C. (b) The performance data in the first one hour. (c) Impedance spectra of the p-SOFC with the PtGa catalyst layer before and after stability test.

4. Conclusion

In this work, we demonstrate the high-performance and stable co-generation of olefin products and electric power in a propane-fueled p-SOFC by incorporating a highly efficient industry-relevant PtGa/ZSM-5 catalyst layer on the anode. Compared with the cells without catalyst or with the conventional perovskite structured PSNT electrocatalyst, superior electrochemical and catalytic performance was successfully achieved by taking advantage of the high activity and selectivity of the thermal catalysts as well as the unique electrochemical performances of proton conducting SOFCs at intermediate temperatures. The PtGa catalyst integrated p-SOFC also exhibits improved carbon tolerance and therefore better stability compared with that without catalyst layer. While discharging current density seemed to have negligible effect on the catalytic performance of the catalyst layer, the propane conversion can be effectively enhanced by applying an overpotential on the catalyst-integrated cells at a certain current density without significantly impacting the olefin product selectivity. It should be stressed that the catalyst-integrated p-SOFC reactor system described in this work is not yet optimized. Therefore, both the electrochemical performance of the p-SOFC and the catalytic performance of the catalyst layer may be further enhanced. For instance, we anticipate that the olefin yield in the catalyst-integrated p-SOFC can be further increased by developing more efficient PDH catalyst and/or loading more catalyst, either via increasing the thickness of the catalyst layer or by employing tubular cells that can accommodate more catalysts than planar cells. The electrochemical performance of the p-SOFC can be improved by developing new electrode/electrolyte materials and optimizing the synthesis and fabrication procedures. Overall, this work provides a general approach for exploiting the potential of solid oxide electrochemical cells in chemical manufacturing by integrating thermal catalysis and electrochemical energy conversion.

CRediT authorship contribution statement

Ruifang Zhang : Writing – original draft, Investigation, Formal analysis, Data curation. **Yuqing Meng :** Investigation, Formal analysis, Data curation. **Lu-Cun Wang :** Writing – review & editing, Supervision, Resources, Project administration, Methodology, Investigation, Funding acquisition, Formal analysis, Data curation, Conceptualization. **Min Wang :** Visualization, Formal analysis, Data curation. **Wei Wu :** Writing – review & editing. **Wenzhuo Wu :** Supervision.

Declaration of Competing Interest

The authors declare that they have no known competing financial interests or personal relationships that could have appeared to influence the work reported in this paper.

Data availability

Data will be made available on request.

Acknowledgements

This work was supported by the U.S. Department of Energy (USDOE), Office of Energy Efficiency and Renewable Energy (EERE), Advanced Manufacturing Office (AMO) R&D Projects Emerging Research Exploration under DOE Idaho Operations Office under Contract No. DEAC07-05ID14517.

Appendix A. Supplementary data

Supplementary data to this article can be found online at https://doi.org/10.1016/j.fuel.2023.129685.

References

[1] Amghizar I, Vandewalle L.A, Van Geem K.M, Marin G.B. New trends in olefin production. Engineering 2017;3:171–8.
[2] Akah A, Al-Ghrami M. Maximizing propylene production via FCC technology. Appl Petrochem Res 2015;5:377–92.
[3] Lavrenov A, Saifulina L, Buluchevskii E, Bogdanets E. Propylene production technology: Today and tomorrow. Catal Ind 2015;7:175–87.
[4] Chen S, Chang X, Sun G, Zhang T, Xu Y, Wang Y, et al. Propane dehydrogenation: catalyst development, new chemistry, and emerging technologies. Chem Soc Rev 2021;50:3315–54.
[5] Sattler J.J, Ruiz-Martinez J, Santillan-Jimenez E, Weckhuysen B.M. Catalytic dehydrogenation of light alkanes on metals and metal oxides. Chem Rev 2014;114:10613–53.
[6] Bian W, Wu W, Wang B, Tang W, Zhou M, Jin C, et al. Revitalizing interface in protonic ceramic cells by acid etch. Nature 2022;604:479–85.
[7] Ding D, Zhang Y, Wu W, Chen D, Liu M, He T. A novel low-thermal-budget approach for the co-production of ethylene and hydrogen via the electrochemical non-oxidative deprotonation of ethane. Energ Environ Sci 2018;11:1710–6.
[8] Li M, Hua B, Wang L.-C, Sugar J.D, Wu W, Ding Y, et al. Switching of metal–oxygen hybridization for selective CO_2 electrohydrogenation under mild temperature and pressure. Nat Catal 2021;4:274–83.
[9] Li M, Hua B, Wu W, Wang L.-C, Ding Y, Welander M.M, et al. Activating nano-bulk interplays for sustainable ammonia electrosynthesis. Mater Today 2022;60:31–40.
[10] Feng W, Wu W, Jin C, Zhou M, Bian W, Tang W, et al. Exploring the structural uniformity and integrity of protonic ceramic thin film electrolyte using wet powder spraying. J Power Sources Adv 2021;11:100067.
[11] Duan C, Tong J, Shang M, Nikodemski S, Sanders M, Ricote S, et al. Readily processed protonic ceramic fuel cells with high performance at low temperatures. Science 2015;349:1321–6.
[12] Wang M, Wang L.-C, Li H, Wu W, Snyder S.W, Gao G, et al. Nanostructured carbon as highly efficient and stable anodes for ethylene production and power generation in protonic ceramic electrochemical cells. Carbon 2022;199:379–86.
[13] Wu W, Wang L.-C, Hu H, Bian W, Gomez J.Y, Orme C.J, et al. Electrochemically Engineered, Highly Energy-Efficient Conversion of Ethane to Ethylene and Hydrogen below 550 °C in a Protonic Ceramic Electrochemical Cell. ACS Catal 2021;11:12194–202.
[14] Zhan Z, Barnett S.A. An octane-fueled solid oxide fuel cell. Science 2005;308:844–7.
[15] Eguchi K, Kojo H, Takeguchi T, Kikuchi R, Sasaki K. Fuel flexibility in power generation by solid oxide fuel cells. Solid State Ion 2002;152:411–6.
[16] Zhan Z, Barnett S.A. Use of a catalyst layer for propane partial oxidation in solid oxide fuel cells. Solid State Ion 2005;176:871–9.
[17] Yang L, Wang S, Blinn K, Liu M, Liu Z, Cheng Z, et al. Enhanced sulfur and coking tolerance of a mixed ion conductor for SOFCs: $BaZr_{0.1}Ce_{0.7}Y_{0.2-x}Yb_xO_{3-\delta}$. Science 2009;326:126–9.
[18] Liu S, Liu Q, Fu X.-Z, Luo J.-L. Cogeneration of ethylene and energy in protonic fuel cell with an efficient and stable anode anchored with in-situ exsolved functional metal nanoparticles. Appl Catal B: Environ 2018;220:283–9.
[19] Shi N, Xue S, Xie Y, Yang Y, Huan D, Pan Y, et al. Co-generation of electricity and olefin via proton conducting fuel cells using $(Pr_{0.3}Sr_{0.7})_{0.9}Ni_{0.1}Ti_{0.9}O_3$ catalyst layers. Appl Catal B: Environ 2020;272:118973.
[20] Liu S, Behnamian Y, Chuang K.T, Liu Q, Luo J.-L. A-site deficient $La_{0.2}Sr_{0.7}TiO_{3-\delta}$ anode material for proton conducting ethane fuel cell to cogenerate ethylene and electricity. J Power Sources 2015;298:23–9.
[21] Liu S, Chuang K.T, Luo J.-L. Double-layered perovskite anode with in situ exsolution of a Co–Fe alloy to cogenerate ethylene and electricity in a proton-conducting ethane fuel cell. ACS Catal 2016;6:760–8.
[22] Ma R, Gao J, Kou J, Dean D.P, Breckner C.J, Liang K, et al. Insights into the nature of selective nickel sites on Ni/Al_2O_3 catalysts for propane dehydrogenation. ACS Catal 2022;12:12607–16.
[23] Nishihara H, Fukura Y, Inde K, Tsuji K, Takeuchi M, Kyotani T. Carbon-coated mesoporous silica with hydrophobicity and electrical conductivity. Carbon 2008;46:48–53.
[24] Peters D, Feinstein L, Peltzer C. On the High-Temperature Electrical Conductivity of Alumina. J Chem Phys 1965;42:2345–6.
[25] Shariaty P, Atkinson J.D, Hashisho Z. Tailoring the electrical resistivity of zeolite Y by carbon addition to allow resistive heating. J Mater Chem A 2018;6:12082–90.
[26] Álvaro M, Cabeza J.F, Fabuel D, García H, Guijarro E, Martínez de Juan J.L. Electrical conductivity of zeolite films: Influence of charge balancing cations and crystal structure. Chem Mater 2006;18:26–33.
[27] Ding H, Wu W, Jiang C, Ding Y, Bian W, Hu B, et al. Self-sustainable protonic ceramic electrochemical cells using a triple conducting electrode for hydrogen and power production. Nat Commun 2020;11:1907.
[28] Wang P, Yao J, Jiang Q, Gao X, Lin D, Yang H, et al. Stabilizing the isolated Pt sites on $PtGa/Al_2O_3$ catalyst via silica coating layers for propane dehydrogenation at low temperature. Appl Catal B: Environ 2022;300:120731.
[29] Morejudo S.H, Zanón R, Escolástico S, Yuste-Tirados I, Malerød-Fjeld H, Vestre P.K, et al. Direct conversion of methane to aromatics in a catalytic co-ionic membrane reactor. Science 2016;353:563–6.
[30] Feng Y, Luo J, Chuang K.T. Conversion of propane to propylene in a proton-conducting solid oxide fuel cell. Fuel 2007;86:123–8.
[31] Feng Y, Luo J, Chuang K.T. Propane dehydrogenation in a proton-conducting fuel cell. J Phys Chem C 2008;112:9943–9.
[32] Wang Z, Wang Z, Yang W, Peng R, Lu Y. Carbon-tolerant solid oxide fuel cells using $NiTiO_3$ as an anode internal reforming layer. J Power Sources 2014;255:404–9.
[33] Zhang L, Yang C, Frenkel A.I, Wang S, Xiao G, Brinkman K, et al. Co-generation of electricity and chemicals from propane fuel in solid oxide fuel cells with anode containing nano-bimetallic catalyst. J Power Sources 2014;262:421–8.
[34] Xue S, Shi N, Wan Y, Xu Z, Huan D, Zhang S, et al. Novel carbon and sulfur-tolerant anode material $FeNi_3$@PrBa(Fe, $Ni)_{1.9}Mo_{0.1}O_{5+\delta}$ for intermediate temperature solid oxide fuel cells. J Mater Chem A 2019;7:21783–93.
[35] Zhang Y, Yu F, Wang X, Zhou Q, Liu J, Liu M. Direct operation of Ag-based anode solid oxide fuel cells on propane. J Power Sources 2017;366:56–64.
[36] Faro M.L, La Rosa D, Nicotera I, Antonucci V, Arico A.S. Electrochemical investigation of a propane-fed solid oxide fuel cell based on a composite Ni–perovskite anode catalyst. Appl Catal B: Environ 2009;89:49–57.
[37] Kwon O, Sengodan S, Kim K, Kim G, Jeong H.Y, Shin J, et al. Exsolution trends and co-segregation aspects of self-grown catalyst nanoparticles in perovskites. Nat Commun 2017;8:15967.
[38] Imbihl R. Electrochemical promotion of catalytic reactions. Prog Surf Sci 2010;

85:241–78.
[39] Katsaounis A. Recent developments and trends in the electrochemical promotion of catalysis (EPOC). J Appl Electrochem 2010;40:885–902.
[40] Dippon M, Babiniec S.M, Ding H, Ricote S, Sullivan N.P. Exploring electronic conduction through $BaCe_xZr_{0.9-x}Y_{0.1}O_{3-d}$ proton-conducting ceramics. Solid State Ion 2016;286:117–21.
[41] Nakamura T, Mizunuma S, Kimura Y, Mikami Y, Yamauchi K, Kuroha T, et al. Energy efficiency of ionic transport through proton conducting ceramic electrolytes for energy conversion applications. J Mater Chem A 2018;6:15771–80.
[42] Vøllestad E, Strandbakke R, Tarach M, Catalán-Martínez D, Fontaine M.-L, Beeaff D, et al. Mixed proton and electron conducting double perovskite anodes for stable and efficient tubular proton ceramic electrolysers. Nat Mater 2019;18:752–9.